


Routing Acoustic Waves via a Metamaterial with Extreme Anisotropy

Liting Wu,¹ Mourad Oudich,^{2,3} Wenkang Cao,¹ Haolin Jiang,¹ Cheng Zhang,¹ Junchen Ke,¹ Jin Yang,¹ Yuanchen Deng,² Qiang Cheng,^{1,*} Tiejun Cui,^{1,†} and Yun Jing^{2,‡}

¹*Department of Radio Engineering, State Key Laboratory of Millimeter Waves, Southeast University, Nanjing 210096, People's Republic of China*

²*Department of Mechanical and Aerospace Engineering, North Carolina State University, Raleigh, North Carolina 27695, USA*

³*Institut Jean Lamour, Université de Lorraine, CNRS, F-54000 Nancy, France*

 (Received 31 May 2019; revised manuscript received 23 August 2019; published 4 October 2019)

Routing and guiding acoustic waves around sharp corners without backscattering losses is of great interest in the acoustics community. Sonic crystals are primarily utilized to design backscattering-immune waveguides. While conventional approaches use defects to guide waves, a considerably more sophisticated and robust approach was recently developed based on topological edge states. Here, we propose a radically different theoretical framework based on extremely anisotropic media for engineering backscattering-immune waveguides. We theoretically derive the exact condition for one-way wave propagation in zigzag paths. While the theoretical underpinning is universal and applicable to acoustic and electromagnetic waves, the experimental validation is conducted using spoof surface acoustic waves. The proposed metamaterial opens up possibilities for wave manipulation and leads to applications in on-chip devices and noise control.

DOI: [10.1103/PhysRevApplied.12.044011](https://doi.org/10.1103/PhysRevApplied.12.044011)

I. INTRODUCTION

Routing and guiding acoustic waves without energy loss is a central topic in both fundamental and applied research of wave manipulation [1–9]. To achieve highly efficient routing of acoustic waves around sharp corners, the issue of acoustic energy loss due to intrinsic backscattering at the interface must be addressed. Utilizing linear defects in sonic crystals (SCs) to guide acoustic waves around sharp corners was first proposed by Torres *et al.* [10]. This design was later optimized by Khelif *et al.* [1] to obtain full-transmission guided waves by harnessing line defects. Alternatively, acoustic metamaterials (AMMs) can give rise to robust wave guiding by leveraging transformation acoustics or near-zero density [8,9]. However, these methods are generally limited to a very narrow operating bandwidth or certain bending angles (usually 90° for defect-based methods). Recently, the field of robust acoustic wave guiding has enjoyed a strong revival, propelled mainly by the advent of nontrivial topological edge states discovered in SCs. A flurry of activity is devoted to engineering topologically protected waveguides for backscattering-immune one-way acoustic propagation [11–22]. However, these waveguides are poorly coupled

to the background media and SCs are wavelength-scaled structures that can become extremely bulky at low frequencies. The foregoing limitations underscore the importance of identifying alternative strategies for robust wave guiding. Additionally, while a majority of previous studies have focused on bulk acoustic waves, the present study addresses another important form of acoustic waves, *i.e.*, spoof surface acoustic waves (SSAWs), although the theory outlined herein is generic to acoustic and even electromagnetic waves. This paper provides a rigorous analysis and demonstration using extremely anisotropic (EA) AMMs for backscattering-immune one-way propagation of SSAWs.

AMMs are rationally designed materials composed of periodic subwavelength unit cells that can be used to manipulate sound waves in unprecedented ways [23–38]. Many promising applications, such as subwavelength imaging [33,34] and acoustic cloaking [35], have been demonstrated. EA AMMs with large values of positive mass densities have been studied in recent years [36–38], and they are best known for their flat equal-frequency contours (EFCs). On the other hand, SSAWs, hosted by various artificial structures, such as one-dimensional (1D) corrugated rigid interfaces [39–43] and two-dimensional (2D) corrugated surfaces or SCs [44–50], have gained attention in the acoustics community. Compared with conventional surface acoustic waves, which stem from the coupling between longitudinal and transverse waves in

*qiangcheng@seu.edu.cn

†tjcui@seu.edu.cn

‡yjing2@ncsu.edu

solids, SSAWs are guided along the interface between the background fluid medium (e.g., air) and a corrugated perfect rigid body (PRB), and this contributes to their unique applications in lab-on-a-chip devices, energy trapping, and sound focusing. An additional benefit of SSAWs is that they provide a fertile ground for investigating a myriad of wave phenomena, since they hold a crucial advantage over bulk acoustic waves: the entire SSAW wave field can be “noninvasively” measured at a plane slightly above the PRB surface; thus, providing a full metamaterial-acoustic interaction map.

Here, we first examine a unique class of 2D extremely anisotropic medium (EAM) for guiding bulk acoustic waves. Homogenization theory is employed to analyze the acoustic characteristics derived from the strong density anisotropy. Several interesting features of these 2D EAMs are discovered through theoretical and numerical investigations. For instance, we find that the propagation route in this type of 2D EAM is independent of the angle of incidence. Meanwhile, these media can be efficiently coupled with the background media under a wide range of incident angles, beam widths, and source locations. More importantly, the exact condition for backscattering-immune propagation in a zigzag path with sharp corners is rigorously established. The generality of the theory further enables us to implement the concept on a small-sized EA AMM for SSAWs, where the entire wave field of interest is experimentally “mapped” and compared with theory and simulation. All results unambiguously demonstrate robust wave guiding around sharp corners.

II. THEORETICAL ANALYSIS

In Fig. 1(a), we define (X_i, Y_i) ($i = 1, 2, \dots, N$) and (x, y) as the local and global coordinate systems. The 2D EAM in local coordinate systems possesses diagonalizable anisotropic mass densities (ρ_X, ρ_Y) , and the bulk modulus, B , is assumed to be scalar. These parameters can be rewritten in the global coordinate system and the corresponding inverse mass density tensors and bulk modulus B_i in region i can be written as [51]

$$\overset{\leftrightarrow}{\rho}_i^{-1} = \begin{bmatrix} \frac{1}{\rho_{xx}^i} & \frac{1}{\rho_{xy}^i} \\ \frac{1}{\rho_{yx}^i} & \frac{1}{\rho_{yy}^i} \end{bmatrix}, \quad (1)$$

$$B_i = B, \quad (2)$$

with

$$\frac{1}{\rho_{xx}^i} = \frac{\cos^2 \alpha_i}{\rho_X} + \frac{\sin^2 \alpha_i}{\rho_Y}, \quad (3)$$

$$\frac{1}{\rho_{yy}^i} = \frac{\cos^2 \alpha_i}{\rho_Y} + \frac{\sin^2 \alpha_i}{\rho_X}, \quad (4)$$

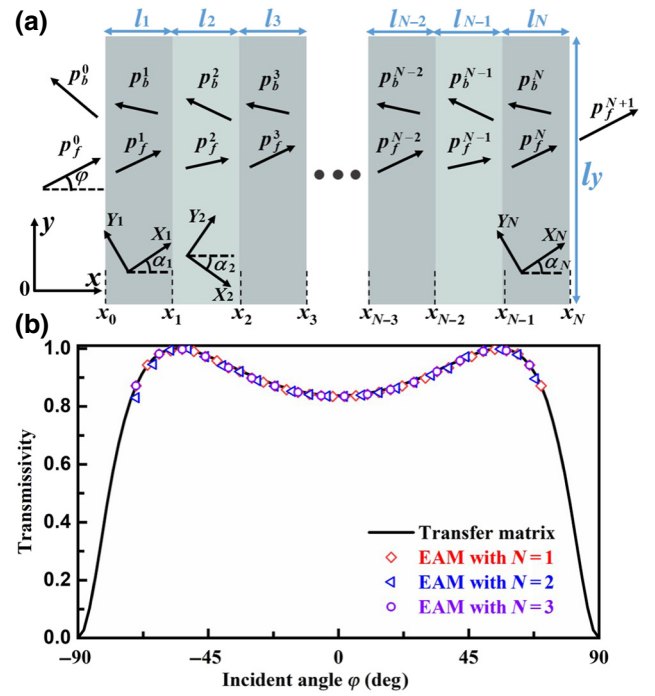


FIG. 1. (a) Schematic of the 2D EAM, consisting of different domains under different local coordinate systems. The interfaces between adjacent domains are located at $x = x_i$ ($i = 1, 2, \dots, N-1$). (b) Simulated transmissivity, T , of the 2D EAMs with $N = 1$ (red diamonds), $N = 2$ (blue triangles), and $N = 3$ (purple circles), and theoretical results calculated by the transfer matrix method. Here, $\Delta x = x_N - x_0 = 600$ mm, $\rho_X = 1.25\rho_0$ and $B = 1.25B_0$. $|\alpha_i| = 45^\circ$ and the operation frequency is 5000 Hz.

$$\frac{1}{\rho_{xy}^i} = \frac{1}{\rho_{yx}^i} = \sin \alpha_i \cos \alpha_i \left(\frac{1}{\rho_X} - \frac{1}{\rho_Y} \right). \quad (5)$$

Here, α_i are the rotation angles of the local coordinate system relative to the global coordinate system [marked in Fig. 1(a)]. It is shown in Sec. II that these angles must be identical in magnitude to ensure backscattering-immune sound propagation. Here, we define that, when the coordinate system (X_i, Y_i) rotates anticlockwise in the xoy plane, the angle of rotation, α_i , is positive; otherwise it is negative. The dispersion relation in the 2D EAM can be obtained as (Appendix A)

$$\frac{(k_i^\pm)^2}{\rho_{xx}^i} + \frac{2k_i^\pm k_y}{\rho_{xy}^i} + \frac{k_y^2}{\rho_{yy}^i} - \frac{\omega^2}{B} = 0, \quad (6)$$

where $k_i^\pm = \pm n_i k - m_i k_y$ are the forward and backward wave numbers with $n_i = \sqrt{\rho_{xx}^i c_0^2 / B - \rho_{xx}^i \sin^2 \varphi / \rho_X \rho_Y}$ and $m_i = \rho_{xx}^i / \rho_{xy}^i$; k is the wave number of the background, and k_y is the component of k in the y direction. The group velocity, \vec{v}_g^i , can be subsequently derived. When the

medium satisfies the condition of the 2D EAM (ρ_X is of a finite value and $\rho_Y \rightarrow \infty$), we have (Appendix A)

$$\vec{v}_g^i = \sqrt{\frac{B}{\rho_X}} \begin{pmatrix} \cos \alpha_i \\ \sin \alpha_i \end{pmatrix}. \quad (7)$$

It is evident that the direction of group velocity depends only on the angles of rotation, α_i , and is insensitive to the incidence angle, φ . Notably, the group velocity $\vec{v}_g \equiv \nabla_{\vec{k}} \omega(\vec{k})$ specifies the direction of energy flow and is not necessarily parallel to the wave vector \vec{k} (or the phase velocity) of the 2D EAM [52]. Therefore, the direction of the energy flow can be predetermined by assigning the desired α_i .

Furthermore, the reflection coefficient, $r_{i'i'}$, and transmission coefficient, $t_{i'i'}$, from region i to i' ($i = i' \pm 1$) can be shown to satisfy (Appendix B)

$$|r_{i'i'}| = \left| \frac{n_i/\rho_{xx}^i - n_{i'}/\rho_{xx}^{i'}}{n_i/\rho_{xx}^i + n_{i'}/\rho_{xx}^{i'}} \right|, \quad |t_{i'i'}| = \left| \frac{2n_i/\rho_{xx}^i}{n_i/\rho_{xx}^i + n_{i'}/\rho_{xx}^{i'}} \right|. \quad (8)$$

Equation (8) is instrumental because it describes the transmission efficiency around sharp corners for the 2D EAM, which is governed by the angle of rotation, α_i (ρ_{xx}^i contains α_i). On the basis Eq. (8), total transmission can be obtained by letting $|\alpha_i| = |\alpha_{i'}|$ (see Appendix B), giving rise to zero reflection. That is, for a zigzag path with $\alpha_i = -\alpha_{i'}$, backscattering-immune transmission in this 2D EAM can be attained. This is not a severe limitation though, since, in theory, any bending angle can be divided into two identical angles (see Appendix G). Figures 2(a)–2(c) illustrate the simulated pressure magnitude field under different angles of incidence at 5000 Hz with $N = 1, 2$, and 3. Here, we set $|\alpha_i| = 45^\circ$, $\Delta x = x_N - x_0 = 600$ mm, $\rho_X = 1.25\rho_0$, and $B = 1.25B_0$ ($\rho_0 = 1.2$ kg/m³ and $B_0 = 1.4 \times 10^5$ Pa; these are the mass density and bulk modulus of air, respectively). The simulations are carried out by COMSOL Multiphysics. The magnitudes of acoustic pressure in 2D EAMs with $|\alpha_i| = |\alpha_{i'}|$ are virtually identical; thus, demonstrating backscattering-immune sound propagation in the 2D EAM under a wide range of incident angles. The white arrows indicate the direction of energy flow, which is dictated only by the angle of rotation, as predicted by theory. Diffraction is strongly suppressed in the metamaterial, as expected, due to the flat EFC derived from the strong density anisotropy [36]. Notably, the acoustic fields shown in left and center of Fig. 2(a) mimic the characteristic of negative refraction, which can be otherwise achieved by double-negative metamaterials [26], hyperbolic metamaterials [33], parity-time symmetric metasurfaces [53], or Weyl phononic crystals [54]. On the other hand, simulation results with $N = 2$, $\alpha_1 = 45^\circ$, and $\alpha_2 = 0^\circ$ are given in

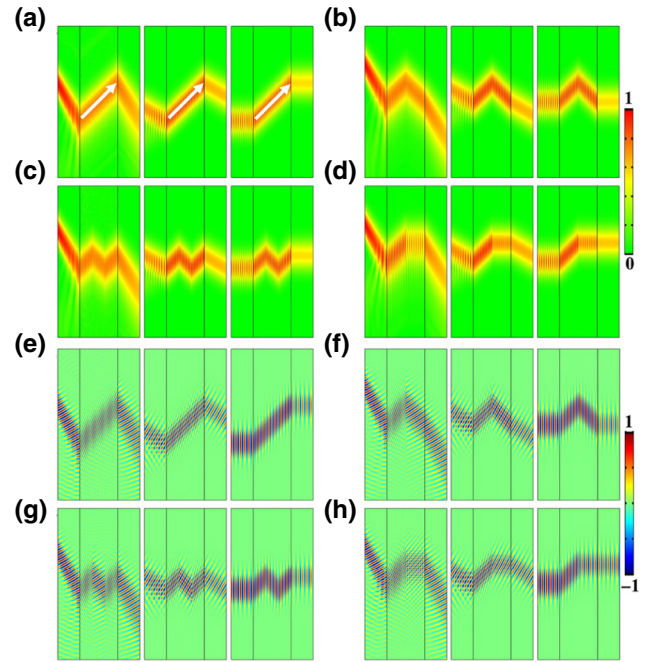


FIG. 2. (a)–(c) The normalized magnitude of the simulated pressure field for the 2D EAM with (a) $N = 1$; (b) $N = 2$, and (c) $N = 3$ under -60° (left), -30° (center), and 0° (right) incidence at 5000 Hz, and $|\alpha_i| = 45^\circ$. (d) The normalized magnitude of the simulated pressure field for the 2D EAM with $\alpha_1 = 45^\circ$, $\alpha_2 = 0^\circ$ and the same change of incident angles. Other parameters are $\Delta x = x_N - x_0 = 600$ mm, $\rho_X = 1.25\rho_0$, and $B = 1.25B_0$. (e)–(h) The real part of the pressure fields in (a)–(d).

Fig. 2(d) for comparison. As expected, energy loss due to backscattering can be seen in this case.

In addition, from the dispersion relation [Eq. (6)], we can obtain the wave numbers in the x direction for the forward and backward waves, i.e., $k_i^\pm = \pm n_i k - m_i k_y$, which suggests that the phase velocities in regions i and i' are different, with $\alpha_i = -\alpha_{i'}$ and $\varphi \neq 0$. However, for the normal incidence case ($\varphi = 0$), we have $k_i^\pm = \pm n_i k$, and therefore, wave vectors (or phase velocities) with $\alpha_i = -\alpha_{i'}$ in regions i and i' are identical. To demonstrate this, Figs. 2(e)–2(h) give the real part of the pressure field shown in Figs. 2(a)–2(d). The phase velocities in neighboring regions are visually different for the oblique incidence case and are identical for the normal incidence, which confirms the theoretical prediction. It is important to point out that the zigzag one-way propagation of sound in this 2D EAM is independent of the location of where the wave impinges upon, since the 2D EAM is a homogeneous medium. On the contrary, the edge state in acoustic topological insulators and valley Hall SCs must be excited by a wave reaching the entrance of the waveguide created by the interface between two topologically distinct SCs. One implication of this is that a wide beam impinging upon a topologically protected waveguide will be largely reflected due to impedance mismatch.

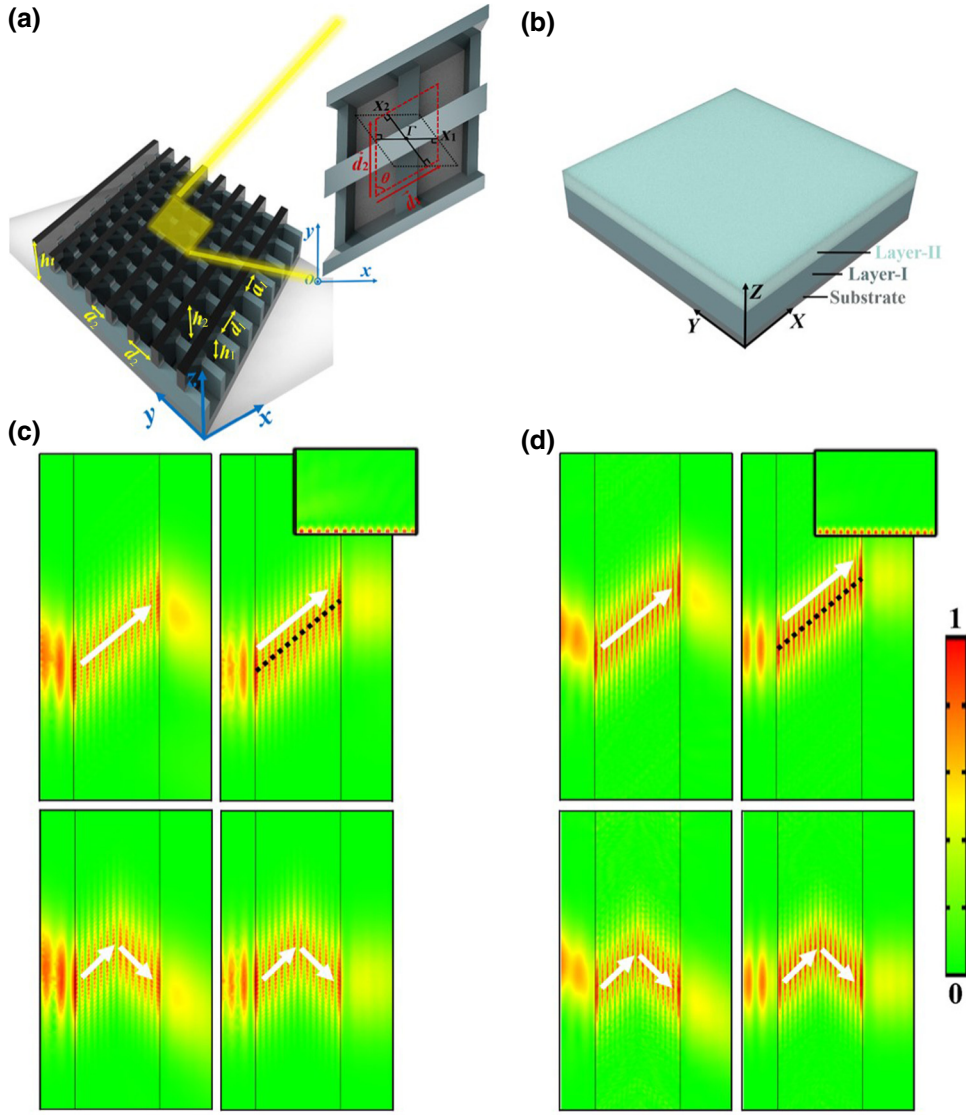


FIG. 3. (a) Schematic of the extremely anisotropic structure for manipulating SSAWs. The structure has heights of h_1 and h_2 along the two directions of the parallelogram sample (PS). h_t is the total height of the structure plus the substrate. The widths of the two grooves are $a_1 = 0.8d_1$ and $a_2 = 0.8d_2$, where d_1 and d_2 are the lattice constants of the unit cell. Inset is an overhead view of part of the structure, which is marked in yellow in (a). θ is the included angle of the two lattice vectors. The first Brillouin zone (FBZ) is depicted by the black dotted line. The unit cell is outlined by the red dashed line. (b) Schematic of the three-layer continuous medium in the local coordinate system. Simulated normalized pressure magnitude field of (c) the PS and (d) the three-layer continuous medium with $|\alpha_i| = 45^\circ$ and $N = 1, 2$ under -30° (left) and 0° (right) incidence at 6000 Hz, which is 0.5 mm above the upper surface of the sample. Here, $d_1 = d_2 = 10$ mm, $a_1 = a_2 = 8$ mm, $h_1 = 10$ mm, and $h_2 = 16$ mm. Insets of (c),(d) are the corresponding pressure magnitude in the cut-plane perpendicular to the xoy plane, with the intersecting line marked by the black dotted line in (c),(d).

Next, we investigate the coupling between the background medium and the 2D EAM shown in Fig. 1(a). The intensity reflectivity, R , and transmissivity, T , at the interface between air and the 2D EAM can be calculated by a transfer matrix method as follows (Appendix C):

$$R = \frac{\left(\xi - \frac{1}{\xi}\right)^2 \sin^2(n_1 k \Delta x)}{\left(\xi + \frac{1}{\xi}\right)^2 \sin^2(n_1 k \Delta x) + 4 \cos^2(n_1 k \Delta x)},$$

$$T = \frac{4}{\left(\xi + \frac{1}{\xi}\right)^2 \sin^2(n_1 k \Delta x) + 4 \cos^2(n_1 k \Delta x)}, \quad (9)$$

where $\xi = \cos \varphi \rho_{xx}^1 / n_1 \rho_0$ and $\Delta x = x_N - x_0$. The reflectivity, R , and transmissivity, T , are independent of N . Figure 1(b) gives the simulated transmissivity of 2D EAM for $N = 1, 2$, and 3, which are in accordance with the theoretical analysis using Eq. (9). Here, all other parameters

are the same as those given above. This suggests, once again, that the sharp corners of a judiciously designed path have virtually no influence on the sound reflectivity and transmissivity. Figure 1(b) also reveals that the 2D EAM can be excellently impedance-matched to the background medium for a wide range of angles of incidence (roughly $-70^\circ \leq \varphi \leq 70^\circ$), and the perfect transmission occurs at an incident angle of $|\varphi| = \arccos(n_1 \rho_0 / \rho_{xx}^1) \approx 50.76^\circ$, which is derived from Eq. (9). This is in stark contrast with acoustic topological insulators and valley Hall SCs, both of which require a specific angle of incidence to achieve momentum matching and efficient acoustic coupling.

III. EXTREMELY ANISOTROPIC ACOUSTIC METAMATERIAL DESIGN

Though backscattering-immune sound propagation can be achieved by the foregoing 2D EAM, challenges in full acoustic field mapping hinder further experimental

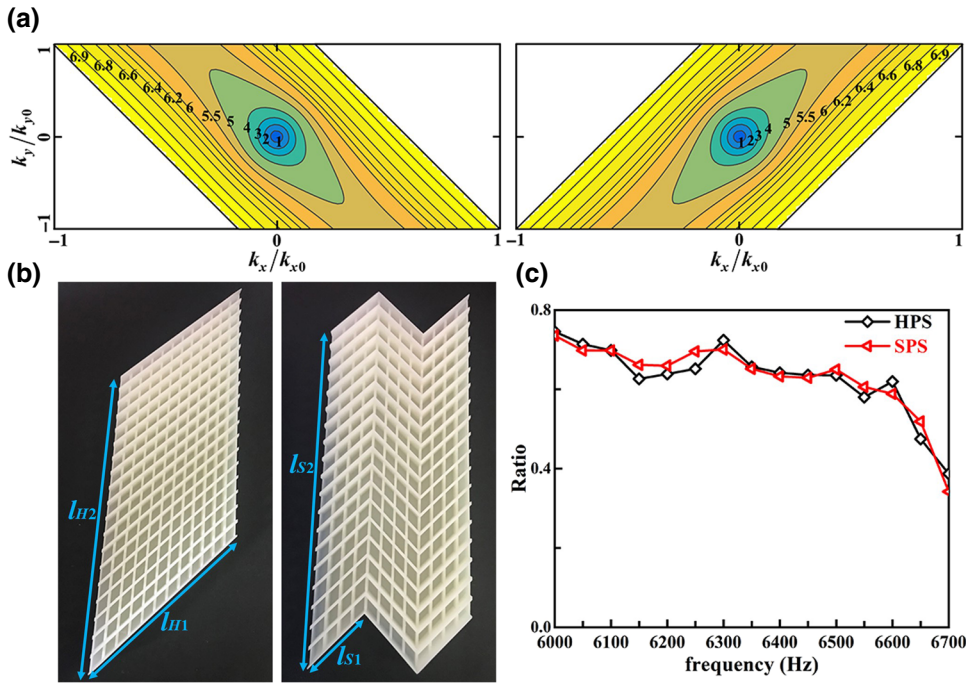


FIG. 4. (a) EFCs in the FBZ of PSs with $\alpha = 45^\circ$ (left) and $\alpha = -45^\circ$ (right), respectively. The frequencies are in kHz. (b) Photographs of the homogeneous PS (HPS; left) and spliced PS (SPS; right). (c) Ratio between the measured energy at the exit of the waveguide and the measured energy at the entrance of the waveguide for both HPS and SPS.

exploration. Consequently, SSAWs are selected in lieu of bulk acoustic waves for validating this design concept. As shown in Fig. 3(a), the proposed EA AMM for manipulating SSAWs can be regarded as two 1D textured PRBs with different heights and orientations crossing each other. Figure 3(a), inset, gives the overhead view of part of the structure, which is marked yellow. The unit cell is outlined by red dashed lines and the lattice constants are indicated in the figure. The lattice vector \vec{d}_2 of the unit cell is along the y direction, and the included angle between the two lattice vectors \vec{d}_1 and \vec{d}_2 is θ . Here, $\theta = 90^\circ - \alpha$ (α is the angle of rotation) and we will adopt α hereafter. To guide acoustic waves along sloping paths or zigzag paths, we must have $|\alpha| > 0^\circ$. Since the overhead view of the sample manifests as a parallelogram, it is denoted as a PS.

To better illustrate the backscattering-immune propagation of SSAWs around sharp corners, we need to determine the anisotropic mass density tensor of the EA AMM under the local coordinate system. To this end, the EA AMM is homogenized as a three-layer continuous acoustic medium, as shown in Fig. 3(b). The substrate is the PRB, while layer-I and layer-II have different material parameters, as follows [36,37]

$$\rho_{X,I} = \rho_{Y,I} = \infty, \quad \rho_{Z,I} = \frac{d_1 d_2}{a_1 a_2} \rho_0 \quad \text{and} \quad B_I = \frac{d_1 d_2}{a_1 a_2} B_0, \quad (10)$$

$$\rho_{X,II} = \rho_{Z,II} = \frac{d_2}{a_2} \rho_0, \quad \rho_{Y,II} = \infty \quad \text{and} \quad B_{II} = \frac{d_2}{a_2} B_0, \quad (11)$$

here, the substrate and layer-I play an important role in confining the direction of SSAWs in the xoy plane.

Layer-II acts as the EAM studied in the Sec. II, routing sound along predetermined paths. Figures 3(c) and 3(d) compare the pressure magnitude distribution at a cut-plane 0.5 mm above the PS and the three-layer continuous medium, with $|\alpha| = 45^\circ$ and $N = 1, 2$ at 6000 Hz. The insets of Figs. 3(c) and 3(d) give the normalized pressure magnitude distribution in the cut-plane, which is perpendicular to the xoy plane, with the intersecting line marked by the black dotted line in Figs. 3(c) and 3(d); this demonstrates that guiding waves of the PS and the three-layer continuous medium are indeed SSAWs, rather than bulk acoustic waves. The detailed geometric parameters are $d_1 = d_2 = 10$ mm, $a_1 = a_2 = 8$ mm, $h_1 = 10$ mm, and $h_2 = 16$ mm. More details regarding the design of this EA AMM can be found in Appendix D. Excellent agreement between the two results clearly demonstrates the incident-angle-independent and backscattering-immune propagation of SSAWs and hereby confirms our theoretical predictions.

EFCs can be further utilized to better understand the characteristics of the proposed SSAW-based PS. Based on the parameters given above, EFCs with $\alpha = \pm 45^\circ$ in the FBZ of the PS are numerically calculated by COMSOL Multiphysics. Here, the FBZ can be obtained by the base vectors of a reciprocal lattice in the xoy plane, i.e., $\vec{\beta}_1 = 2\pi/(d_1 \sin \theta)\hat{x}$ and $\vec{\beta}_2 = 2\pi/(d_2 \sin \theta)\hat{x}'$. \hat{x} and \hat{x}' are unit vectors in the ΓX_1 and ΓX_2 directions, which are perpendicular to \vec{d}_2 and \vec{d}_1 , respectively [shown in the inset of Fig. 3(a)]. Thus, the corresponding FBZ of the PSs with $\alpha = \pm 45^\circ$ is the overlapped area of two different wave vectors with different ranges and directions, i.e., $\beta_1 \in [-\sqrt{2}\pi/d_1, \sqrt{2}\pi/d_1]$ in the \hat{x} direction and $\beta_2 \in$

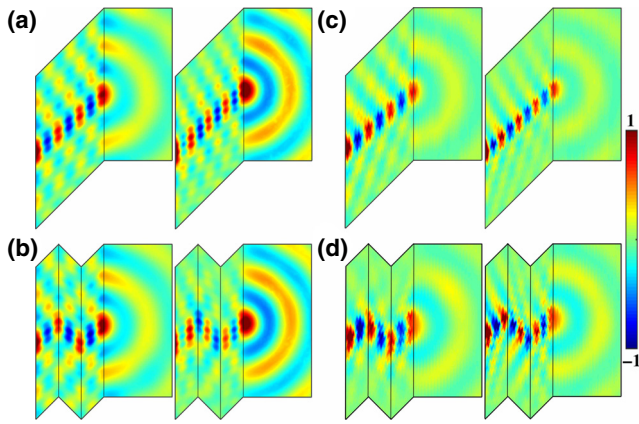


FIG. 5. (a),(b) Simulated and (c),(d) measured pressure field distribution for the domain 0.5 mm above the upper surface of the sample at 6150 Hz (left column) and 6550 Hz (right column).

$[-\sqrt{2}\pi/d_2, \sqrt{2}\pi/d_2]$ in the \hat{x}' direction, which is outlined by black dotted lines. In Fig. 4(a), $k_{x0} = \sqrt{2}\pi/d_1 + \pi/2d_2$ and $k_{y0} = \pi/2d_2$, which correspond to the maximum values of wave numbers in the x and y directions, respectively. The EFCs of the PSs are approximately elliptical at low frequencies, where the two 1D corrugated structures can both support propagating SSAWs, but have different group velocities due to different dispersion relations. As the frequency increases, the EFC transforms from being elliptical to approximately two flat lines, which is a direct manifestation of EAMs. In this case, only those SSAWs propagating in the \vec{d}_1 direction can be supported, and the direction of the energy flow is independent of the angle of incidence, as shown in Figs. 3(c) and 3(d).

IV. EXPERIMENTAL VERIFICATION

Due to the flat EFCs, sound collimation within a wide variety of paths can be expected by PSs, such as sloping and zigzag paths. Figure 4(b) shows a HPS with a sloping path and a SPS with a zigzag path. For the HPS, we set $\alpha = 45^\circ$, and in the two lattice vector directions, we have $l_{H1} = 12d_1$ and $l_{H2} = 19d_2$, respectively. The SPS is constructed by combining three HPSs with successive angles of rotation $\alpha = 45^\circ, -45^\circ, \text{ and } 45^\circ$. The three HPSs have the same length, i.e., $l_{S1} = l_{H1}/3$ and $l_{S2} = 19d_2$. These two samples are made of a photopolymer plate with an array of periodic parallelogram holes, and the heights of the parallelogram hole in the two directions are different. The detailed experimental setup can be found in Appendix E.

In Fig. 4(a), the flat EFCs at higher frequencies, which are parallel to ΓX_2 , can be observed due to the extreme anisotropy of the AMM. Figure 5(a) gives the simulated pressure fields of the HPS at two selected frequencies that exhibit flat EFCs: 6150 and 6550 Hz. The results clearly demonstrate sound collimation. The energy is confined in a waveguide that is roughly 30 mm wide, which is about

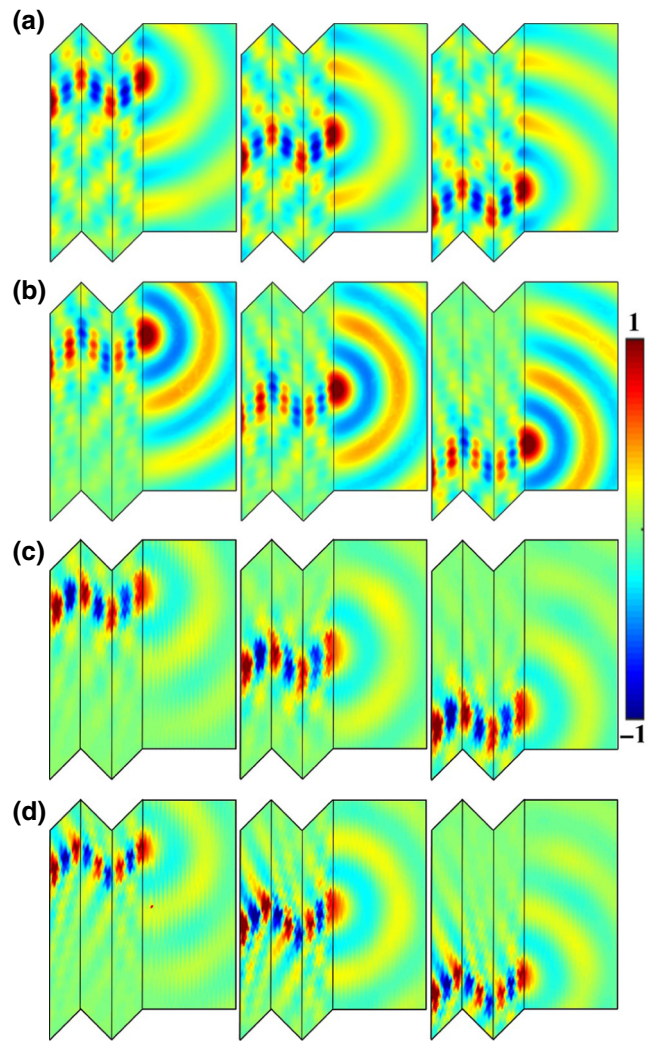


FIG. 6. (a),(b) Simulated and (c),(d) measured pressure field distributions for the domain 0.5 mm above the upper surface of the SPS with the source at different positions on the y axis [50 mm above the center (left column), center (center column), and 50 mm below the center (right column)] at different frequencies: (a),(c) 6150 Hz and (b),(d) 6550 Hz.

half of the wavelength at 6150 Hz measured in free air, i.e., 56 mm. This “subwavelength” feature of the waveguide can be attributed to the fact that the corrugated rigid surface significantly slows down the speed of sound [48]. Measured results, as shown in Fig. 5(c), are, in principle, in good agreement. The slight difference is expected to be caused by sample defects and thermoviscous losses, which are not considered in the simulation.

Remarkably, collimation in a backscattering-immune zigzag path can be observed with the SPS, which is illustrated in Figs. 5(b) and 5(d), respectively, for simulations and measurements. Such a phenomenon can be explained as follows: first, the extreme anisotropy of the textured surface engenders collimation of SSAWs, so that the energy is strongly confined and travels along the predetermined

path. Second, the judiciously designed angles of rotation ensure that backscattering at the corners can be perfectly suppressed, as predicted by the theory established by this work. To further prove that there is no backscattering at the sharp corners, Fig. 4(c) compares the transmitted sound energy between the HPS (no bending) and SPS (with bending). Notably, the two waveguides have identical lengths and virtually the same sound transmission can be seen, even though the SPS contains sharp corners. Here, the relatively low measured transmittances of the two samples can be ascribed to thermoviscous losses. One important observation is that the size of the wave-guiding EA AMM is very small, relative to the wavelength in free air; for example, the width of the EA AMM, l_{H2}/l_{S2} , is merely 3.4 wavelengths at 6150 Hz. Additional simulations show that l_{S2} can be reduced by more than half ($l_{S2} = 1.6$ wavelengths) and the resulting EA AMM will still yield excellent performance (Appendix F). Finally, we highlight two important facts: (1) sloping and zigzag paths with arbitrary angles are feasible using the current design scheme; some results are shown in Appendix F to support this point; and (2) as predicted by theory, this EA AMM can be efficiently coupled with acoustic sources almost arbitrarily located along the vertical direction, offering the possibility that the sound propagation path can be tuned flexibly by adjusting the source position. Relevant simulation and experimental results are shown in Fig. 6.

V. CONCLUSION

In summary, we devise and experimentally demonstrate an alternative class of EA AMM that supports backscattering-immune wave propagation around sharp corners. Based on the wave and Helmholtz equation and homogenization theory, we theoretically derive the exact conditions for perfect suppression of backscattering in zigzag paths with sharp corners. Our proposed wave guiding strategy hinges on the use of metamaterials that exhibit strong anisotropy and is numerically and experimentally shown to support robust one-way propagation in zigzag paths. While this study focuses on sawtooth-like zigzag waveguides, other types of waveguides with sharp corners can be designed and demonstrated (Appendix G). One limitation of our design is that the bending angles at the corners have to be identical. This is, however, only a limitation for the SSAW AMM design and does not apply to the effective medium and bulk acoustic wave EA AMMs (Appendix G). Additionally, it must be pointed out that, unlike acoustic topological insulators, which are robust against a large class of defects [55], the proposed structure works only for zigzag waveguides. Finally, the theory established in this work is generic and can be extended to electromagnetic waves (Appendix H). Our proposed method could be useful for many applications, such as

delay line design, noise control, acoustic cloaking, and on-chip wave manipulation [40–43,45–48].

ACKNOWLEDGMENTS

This work is supported by the National Key Research and Development Program of China (Grants No. 2017YFA0700201, No. 2017YFA0700202, and No. 2017YFA0700203), the National Natural Science Foundation of China (Grants No. 61722106 and No. 61731010), the 111 Project (Grant No. 111-2-05), and the Postgraduate Research & Practice Innovation Program of Jiangsu Province (Grant. No. KYCX18_0099).

APPENDIX A: THE ANALYSIS OF INCIDENT-ANGLE-INDEPENDENT SLOPING PATH BY EXTREMELY ANISOTROPIC MEDIA

To investigate the underlying physics of the sloping path, we give the analysis of 2D EAM first. The configuration is shown in Fig. 7(a), which possesses the mass density tensor $\overset{\leftrightarrow}{\rho}^{\text{diag}}$ with nonzero diagonal elements (the bulk modulus, B , is assumed to be a scalar) as follows:

$$\overset{\leftrightarrow}{\rho}^{\text{diag}} = \begin{bmatrix} \rho_X & 0 \\ 0 & \rho_Y \end{bmatrix}, \quad (\text{A1})$$

where X and Y are the two components in the local coordinate system marked in Fig. 7(a). In the global coordination system (x, y) , the inverse mass density tensors can be obtained by rotational operators R and they are calculated to be [51]

$$\overset{\leftrightarrow}{\rho}^{-1} = \begin{bmatrix} \frac{1}{\rho_{xx}} & \frac{1}{\rho_{xy}} \\ \frac{1}{\rho_{yx}} & \frac{1}{\rho_{yy}} \end{bmatrix}, \quad (\text{A2})$$

with

$$R = \begin{pmatrix} \cos \alpha & -\sin \alpha \\ \sin \alpha & \cos \alpha \end{pmatrix}, \quad (\text{A3})$$

and

$$\frac{1}{\rho_{xx}} = \frac{\cos^2 \alpha}{\rho_X} + \frac{\sin^2 \alpha}{\rho_Y}, \quad (\text{A4})$$

$$\frac{1}{\rho_{yy}} = \frac{\cos^2 \alpha}{\rho_Y} + \frac{\sin^2 \alpha}{\rho_X}, \quad (\text{A5})$$

$$\frac{1}{\rho_{xy}} = \frac{1}{\rho_{yx}} = \sin \alpha \cos \alpha \left(\frac{1}{\rho_X} - \frac{1}{\rho_Y} \right). \quad (\text{A6})$$

Here, we define that, when the coordinate system (X, Y) rotates anticlockwise, the angle of rotation, α , is positive;

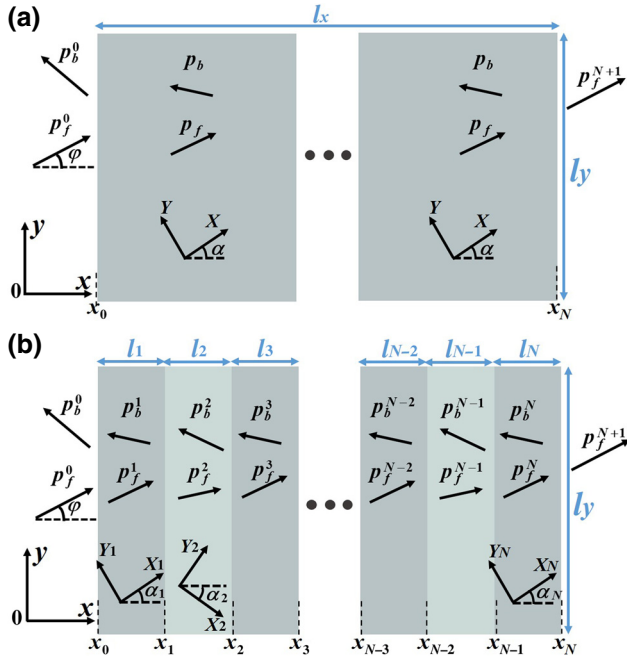


FIG. 7. Schematic of the 2D EAM with (a) sloping path and (b) zigzag paths. The total reflection coefficient, r , and transmission coefficient, t , of the sample are calculated by the transfer matrix method. Each interface located at $x = x_i$ ($i = 1, 2, \dots, N-1$) can be treated as a secondary plane source. The angle and wave number of the obliquely incident plane wave are φ and k , respectively.

otherwise it is negative. For an arbitrary plane wave incident from air, the pressure field inside and outside the 2D EAM can be given as

$$p(x \leq x_0) = p_f^0 + p_b^0 = e^{jk_y y + jk_x x} + r e^{jk_y y - jk_x x}, \quad (\text{A7})$$

$$p(x_0 < x \leq x_N) = p_f + p_b = F e^{jk_y y + jk^+ x} + B e^{jk_y y + jk^- x}, \quad (\text{A8})$$

$$p(x_N \leq x) = p_f^{N+1} = t e^{jk_y y + jk_x x}, \quad (\text{A9})$$

with $k_x = k \cos \varphi$ and $k_y = k \sin \varphi$; F , B , and k^\pm are the coefficients and horizontal wave numbers of the forward- and backward-traveling waves; r and t are the total reflection coefficient and transmission coefficient, respectively, at the interface between air and the 2D EAM. The acoustic pressure field, p , for the 2D EAM satisfies the wave equation $\nabla[\rho \nabla p] + (c_0^2 k^2 / B)p = 0$; after inserting the pressure field distribution, the dispersion relation can be obtained as

$$\frac{(k^\pm)^2}{\rho_{xx}} + \frac{2k^\pm k_y}{\rho_{xy}} + \frac{k_y^2}{\rho_{yy}} - \frac{\omega^2}{B} = 0, \quad (\text{A10})$$

leading to

$$k^\pm = \pm nk - mk_y, \quad \text{with } n \equiv \sqrt{\frac{\rho_{xx} c_0^2}{B} - \frac{\rho_{xx}^2 \sin^2 \varphi}{\rho_X \rho_Y}} \quad \text{and} \\ m = \frac{\rho_{xx}}{\rho_{xy}}. \quad (\text{A11})$$

Meanwhile, the relationship between the direction of energy and phase velocity can be given by the group velocity $\vec{v}_g \equiv \nabla_{\vec{k}} \omega(\vec{k})$ [52],

$$\vec{v}_g = \frac{1}{\sqrt{B \left[\frac{(k^\pm)^2}{\rho_{xx}} + \frac{2k^\pm k_y}{\rho_{xy}} + \frac{k_y^2}{\rho_{yy}} \right]}} \begin{pmatrix} \frac{k_x}{\rho_{xx}} + \frac{k_y}{\rho_{xy}} \\ \frac{k_x}{\rho_{xy}} + \frac{k_y}{\rho_{yy}} \end{pmatrix}. \quad (\text{A12})$$

For the case where ρ_X is of a finite value and $\rho_Y \rightarrow \infty$ (or $1/\rho_Y \rightarrow 0$), the group velocity can be simplified as

$$\vec{v}_g = \sqrt{\frac{B}{\rho_X}} \begin{pmatrix} \cos \alpha \\ \sin \alpha \end{pmatrix}. \quad (\text{A13})$$

It is clear that the direction of energy flow depends only on the angle of rotation, α , and is independent of the angle of incidence, φ .

APPENDIX B: THE ANALYSIS OF BACKSCATTERING-IMMUNE ZIGZAG PATHS BY EXTREMELY ANISOTROPIC MEDIA

In addition to simple sloping paths in the 2D EAM, zigzag paths are also discussed here. As shown in Fig. 7(b), the medium with $\rho_{Y_i} = \rho_Y$ and $\rho_{X_i} = \rho_X$ ($i = 1, 2, \dots, N-1$) is composed of N parts. The neighboring parts have different angles of rotation. The inverse mass density tensors for these regions can be rewritten as

$$\overset{\leftrightarrow}{\rho}_i^{-1} = \begin{bmatrix} \frac{1}{\rho_{xx}^i} & \frac{1}{\rho_{xy}^i} \\ \frac{1}{\rho_{xy}^i} & \frac{1}{\rho_{yy}^i} \end{bmatrix}. \quad (\text{B1})$$

The directions of phase velocities can be obtained by the wave numbers $k_{y,i} = k_y$ and $k_i^\pm = \pm n_i k - m_i k_y$, with $n_i \equiv \sqrt{\rho_{xx}^i c_0^2 / B - (\rho_{xx}^i)^2 \sin^2 \varphi / \rho_X \rho_Y}$ and $m_i \equiv \rho_{xx}^i / \rho_{xy}^i$. The acoustic pressure field in the regions of 2D EAM can be replaced by

$$p(x_{i-1} < x \leq x_i) = p_f^i + p_b^i = F_i e^{jk_y y + jk_i^+ x} + B_i e^{jk_y y + jk_i^- x}. \quad (\text{B2})$$

Based on the relation $\vec{v} = (1/j\omega)\overleftrightarrow{\rho}^{-1} \nabla p$, the acoustic velocity in the x direction can be obtained as follows:

$$\begin{aligned} v_{xi} &= \frac{1}{j\omega} \left(\frac{1}{\rho_{xx}^i} \frac{\partial p}{\partial x} + \frac{1}{\rho_{xy}^i} \frac{\partial p}{\partial y} \right) \\ &= \frac{1}{\rho_{xx}^i} \frac{n_i k}{\omega} e^{jk_y y} (F_i e^{jk_i^+ x} - B_i e^{jk_i^- x}). \end{aligned} \quad (\text{B3})$$

The relationships of coefficient (F_i and B_i) for the forward and backward-traveling waves in the neighboring regions can be derived by applying the matching boundary conditions for p and v_x (v_x and p are continuous at the interface $x = x_i$, $i = 1, 2, \dots, N-1$). We then have

$$F_i e^{jk_i^+ x_i} + B_i e^{jk_i^- x_i} = F_{i'} e^{jk_{i'}^+ x_i} + B_{i'} e^{jk_{i'}^- x_i}, \quad (\text{B4})$$

$$\frac{1}{\rho_{xx}^i} \frac{n_i}{c_0} (F_i e^{jk_i^+ x_i} - B_i e^{jk_i^- x_i}) = \frac{1}{\rho_{xx}^{i'}} \frac{n_{i'}}{c_0} (F_{i'} e^{jk_{i'}^+ x_i} - B_{i'} e^{jk_{i'}^- x_i}). \quad (\text{B5})$$

Therefore, the reflection coefficient, $r_{i'}$, and transmission coefficient, $t_{i'}$, from region i to i' ($i = i' \pm 1$) can be obtained:

$$|r_{i'}| = \left| \frac{n_i/\rho_{xx}^i - n_{i'}/\rho_{xx}^{i'}}{n_i/\rho_{xx}^i + n_{i'}/\rho_{xx}^{i'}} \right|, \quad |t_{i'}| = \left| \frac{2n_{i'}/\rho_{xx}^{i'}}{n_i/\rho_{xx}^i + n_{i'}/\rho_{xx}^{i'}} \right|. \quad (\text{B6})$$

To avoid backscattering between the neighboring regions, we must have $n_i/\rho_{xx}^i - n_{i'}/\rho_{xx}^{i'} = 0$, which means that $|\alpha_i| = |\alpha_{i'}|$. For a zigzag path, we can design the path so that $\alpha_i = -\alpha_{i'}$. Here, we note that $|\alpha_i| = |\alpha_{i'}|$ is the exact solution of $r_{i'} = 0$, without imposing any restraint on ρ_Y , which means that this conclusion can be generalized to the case where ρ_Y is of a finite value. Additionally, the backscattering-immune zigzag path can be easily shown to be independent of the angle of incidence.

APPENDIX C: MODELING USING THE TRANSFER MATRIX METHOD

The pressure reflectivity, R , and transmissivity, T , at the interface between air and the 2D EAM are analyzed here. We give an illustration from the view of a multiple-transmission process, in which each interface of the 2D EAM can be regarded as a secondary plane source. As shown in Fig. 7(b), the pressures and normal component of particle velocities on both sides of the layer are related via a transfer matrix \overleftrightarrow{M}_i ($i = 1, 2, \dots, N$)

$$\begin{bmatrix} p(x_i) \\ v_x(x_i) \end{bmatrix} = \overleftrightarrow{M}_i \begin{bmatrix} p(x_{i-1}) \\ v_x(x_{i-1}) \end{bmatrix}, \quad (\text{C1})$$

where

$$\overleftrightarrow{M}_i = \begin{bmatrix} \cos(n_i k l_i) e^{-j m_i k y l_i} & j \frac{\rho_{xx}^i c_0}{n_i} \sin(n_i k l_i) e^{-j m_i k y l_i} \\ j \frac{n_i}{\rho_{xx}^i c_0} \sin(n_i k l_i) e^{-j m_i k y l_i} & \cos(n_i k l_i) e^{-j m_i k y l_i} \end{bmatrix}. \quad (\text{C2})$$

For 2D EAMs consisting of N layers, the overall transfer matrix in the forward direction can be written in the form

$$\overleftrightarrow{M} = \overleftrightarrow{M}_N \times \dots \times \overleftrightarrow{M}_3 \times \overleftrightarrow{M}_2 \times \overleftrightarrow{M}_1. \quad (\text{C3})$$

The reflection, r , and transmission, t , coefficients can be obtained from the elements in \overleftrightarrow{M} as

$$\begin{aligned} r &= \frac{M_{11} + \frac{\cos \varphi}{\rho_0 c_0} M_{12} - \frac{\rho_0 c_0}{\cos \varphi} M_{21} - M_{22}}{-M_{11} + \frac{\cos \varphi}{\rho_0 c_0} M_{12} + \frac{\rho_0 c_0}{\cos \varphi} M_{21} - M_{22}} e^{j 2 k_x x_0}, \\ t &= \frac{2(M_{12} M_{21} - M_{11} M_{22}) e^{-j k_x \Delta x}}{-M_{11} + \frac{\cos \varphi}{\rho_0 c_0} M_{12} + \frac{\rho_0 c_0}{\cos \varphi} M_{21} - M_{22}}, \end{aligned} \quad (\text{C4})$$

where ρ_0 and c_0 are the density and speed of sound in air, respectively; $\Delta x = x_N - x_0$ is the total length of sample in the x direction. We then use the transfer matrix method to examine the overall pressure reflection and transmission coefficients:

$$\begin{aligned} r &= \frac{j \left(\frac{\cos \varphi \rho_{xx}^1}{n_1 \rho_0} - \frac{n_1 \rho_0}{\cos \varphi \rho_{xx}^1} \right) \sin(n_1 k \Delta x) e^{j 2 k_x x_0}}{j \left(\frac{\cos \varphi \rho_{xx}^1}{n_1 \rho_0} + \frac{n_1 \rho_0}{\cos \varphi \rho_{xx}^1} \right) \sin(n_1 k \Delta x) - 2 \cos(n_1 k \Delta x)}, \\ t &= \frac{-2 e^{-j m_1 k_y \delta x} e^{-j k_x \Delta x}}{j \left(\frac{\cos \varphi \rho_{xx}^1}{n_1 \rho_0} + \frac{n_1 \rho_0}{\cos \varphi \rho_{xx}^1} \right) \sin(n_1 k \Delta x) - 2 \cos(n_1 k \Delta x)}, \end{aligned} \quad (\text{C5})$$

with $\delta x = l_1 - l_2 + l_3 - \dots + (-1)^{N+1} l_N$ for backscattering-immune zigzag paths and $\delta x = \Delta x$ for sloping paths. Correspondingly, the intensity reflection coefficient, $R = |r|^2$, and intensity transmission coefficient, $T = |t|^2$, can be obtained

$$\begin{aligned} R &= \frac{\left(\frac{\cos \varphi \rho_{xx}^1}{n_1 \rho_0} - \frac{n_1 \rho_0}{\cos \varphi \rho_{xx}^1} \right)^2 \sin^2(n_1 k \Delta x)}{\left(\frac{\cos \varphi \rho_{xx}^1}{n_1 \rho_0} + \frac{n_1 \rho_0}{\cos \varphi \rho_{xx}^1} \right)^2 \sin^2(n_1 k \Delta x) + 4 \cos^2(n_1 k \Delta x)}, \\ T &= \frac{4}{\left(\frac{\cos \varphi \rho_{xx}^1}{n_1 \rho_0} + \frac{n_1 \rho_0}{\cos \varphi \rho_{xx}^1} \right)^2 \sin^2(n_1 k \Delta x) + 4 \cos^2(n_1 k \Delta x)}. \end{aligned} \quad (\text{C6})$$

It is easy to find that R and T are independent of N for a

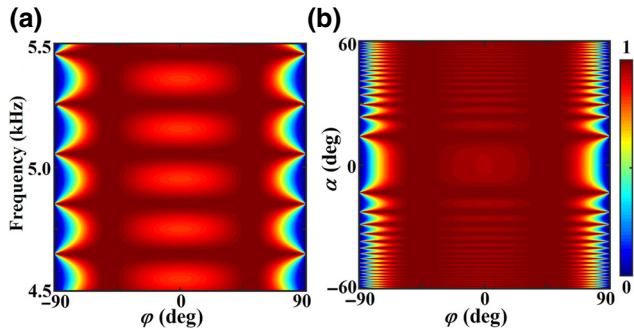


FIG. 8. (a) The transmissivity, T , as a function of incident angle, φ , and operating frequency with $\alpha = 45^\circ$. (b) The transmissivity, T , as a function of incident angle, φ , and angle of rotation, α , at 5000 Hz. Other parameters are $\Delta x = 600$ mm, $\rho_X = 1.25\rho_0$, and $B = 1.25B_0$.

given Δx , i.e., the total transmissivities are identical for the 2D EAMs with backscattering-immune zigzag paths and sloping paths, as long as they have the same length in the x direction. Meanwhile, the transmissivity possesses periodic variation as the operating frequency increases. Figure 8(a) gives the transmissivities versus incident angle, φ , and operating frequency using Eq. (C6), where it is assumed

that $\Delta x = x_N - x_0 = 600$ mm, $\rho_X = 1.25\rho_0$, $B = 1.25B_0$, and $|\alpha_i| = 45^\circ$. The transmissivity at 5000 Hz as a function of the incident angle, φ , and rotation angle, α , is given in Fig. 8(b).

APPENDIX D: PROPAGATION FEATURES OF SPOOF SURFACE ACOUSTIC WAVES SUPPORTED BY THE HOMOGENEOUS PARALLELOGRAM SAMPLE

To explore the propagation features of SSAWs of the EA AMMs, we take the HPS with $\alpha = 45^\circ$ for simple analysis. As shown in Fig. 3(a), the HPS can be regarded as two 1D textured PRBs with different heights and orientations crossing each other. The cutoff frequencies of the two 1D textured PRBs are critical for analyzing the acoustical properties of this EA AMM, which can be obtained by the dispersion relation of 1D SSAWs as follows [39]:

$$\sqrt{k_{t,i}^2 - k_{o,i}^2}/k_{o,i} = \frac{a_i}{d_i} \tan(k_{o,i}h_i), \quad i = 1 \text{ or } 2, \quad (\text{D1})$$

where $k_{t,i}$ and $k_{o,i}$ are the propagating and operating wave numbers, respectively. Figure 9(a) gives the dispersion curves with different geometrical parameters. The corresponding cutoff frequencies can be readily calculated and

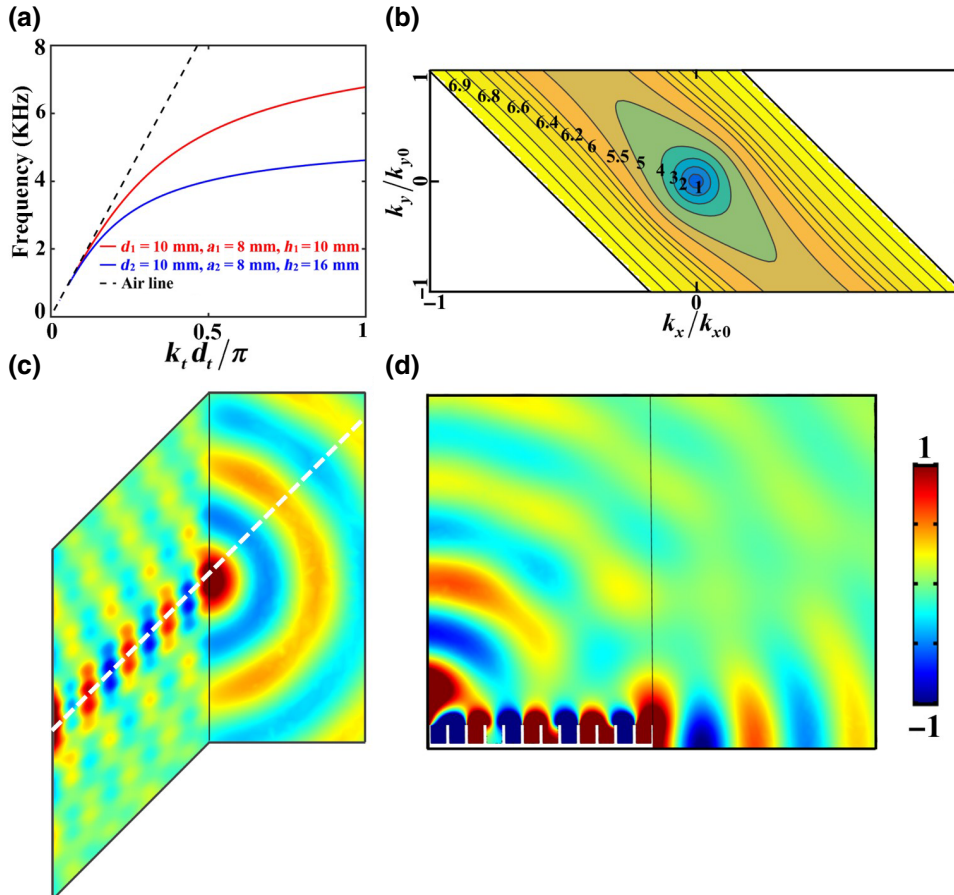


FIG. 9. (a) Dispersion relations of the two 1D textured PRB with different heights (bottom PRB in red and upper PRB in blue). (b) EFCs in FBZ of the HPS with $\alpha = 45^\circ$. The frequency values are in kHz. Simulated acoustic pressure field of the HPS at 6550 Hz in (c) xoy plane (0.5 mm above the upper surface of the HPS) and (d) cut-plane, which is perpendicular to the xoy plane with the intersecting line marked by the white dashed line in (c).

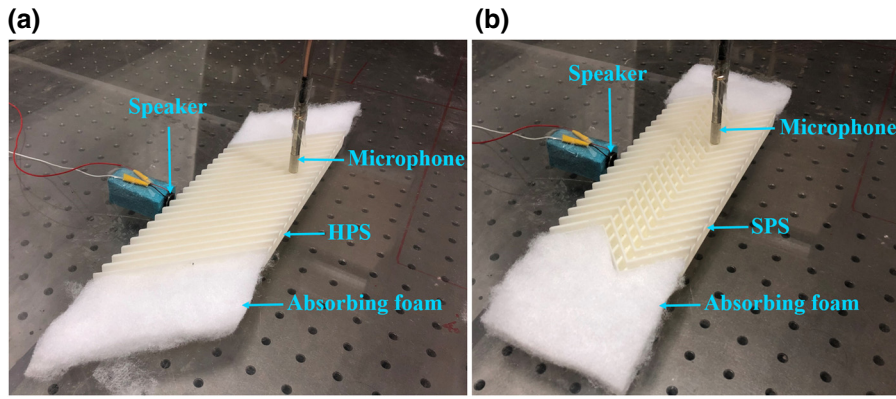


FIG. 10. The experimental setup for testing the extremely anisotropic meta-material for controlling SSAWs with (a) sloping and (b) backscattering-immune zigzag paths. The microphone is placed 0.5 mm above the upper surface of sample.

are $f_1 = 6768$ Hz and $f_2 = 4610$ Hz. Theoretically, when the operating frequency f_o satisfies $f_o < f_2 < f_1$, SSAWs propagate along both directions, and EFCs are approximately elliptical due to the anisotropy of the material. When the operating frequency f_o satisfies $f_2 < f_o < f_1$, only SSAWs propagating along the \vec{d}_1 direction can be supported. Figure 9(b) gives the EFCs in FBZ of the HPS, which is numerically calculated by COMSOL Multiphysics. At low frequencies, the elliptical EFCs of the PS demonstrate the propagating SSAWs in all directions. As the frequency increases, only SSAWs propagating in the \vec{d}_1 direction can be excited due to the flat EFCs, and the direction of the energy flow is independent of the incident angle.

Sound collimation with a sloping path can be created by the HPS at frequencies where the flat EFCs are displayed. Figure 9(c) gives the simulated acoustic pressure fields in the xoy plane, which is 0.5 mm above the upper surface of the HPS, at 6550 Hz. The group velocity vectors are perpendicular to the EFC, which is flat; thus, the acoustic wave propagates along the \vec{d}_1 direction in a self-collimating manner. To verify the characteristics of SSAWs, Fig. 9(d) gives the simulated acoustic pressure field at 6550 Hz in the cut-plane, which is perpendicular to the xoy plane, with the intersecting line marked by the white dashed line in Fig. 9(c). It is clear that the energy of sound is confined to the top surface of the HPS, until reaching the end of the structure.

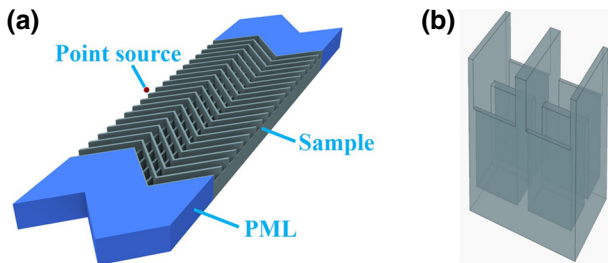


FIG. 11. (a) The simulated setup for the EA AMM. (b) The perspective of part of the sample. PML: perfectly matched layer.

APPENDIX E: EXPERIMENTAL AND SIMULATION SETUP FOR THE HOMOGENOUS PARALLELOGRAM SAMPLE AND SPLICED PARALLELOGRAM SAMPLE

Figure 10 shows the experimental setup for wave guiding with sloping paths by the HPS and backscattering-immune paths by the SPS, where a speaker with a radius of $r = 5$ mm, mimicking a point source, is placed 5 mm away from the front face of the sample to excite the SSAWs. Sound-absorbing foams are placed on two sides of the sample to minimize reflection and sound field interference. The scan area contains two domains that are 0.5 mm above the upper surface of the sample: one is the region directly above the sample and the other one is a rectangular region

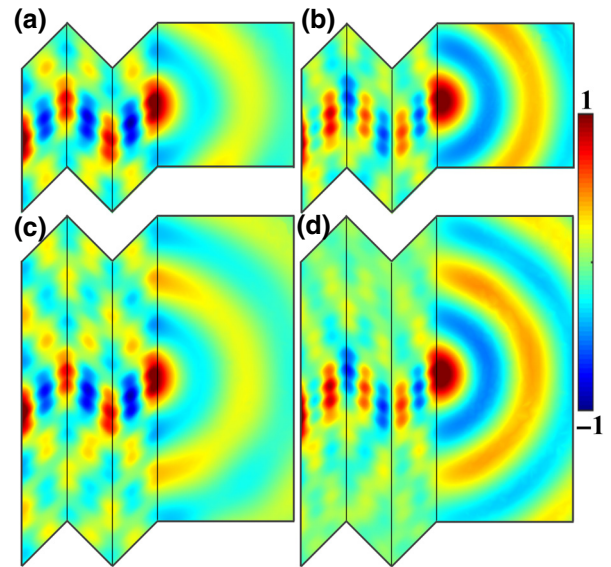


FIG. 12. Simulated pressure field distribution for the domain 0.5 mm above the upper surface of the SPS with different widths in y axis (a),(b) $l_{S2} = 90$ mm and (c),(d) $l_{S2} = 190$ mm at different frequencies. (a),(c) 6150 Hz and (b),(d) 6550 Hz. Other parameters are the same as those in Figs. 3(a) and 4(b) ($d_1 = d_2 = 10$ mm, $a_1 = a_2 = 8$ mm, $h_1 = 10$ mm, $h_2 = 16$ mm, $l_{S1} = 40$ mm, and $\alpha_1 = -\alpha_2 = \alpha_3 = 45^\circ$).

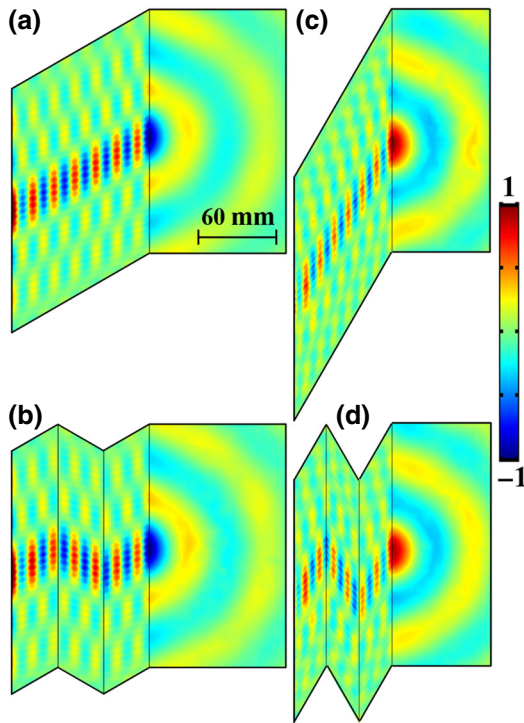


FIG. 13. Simulated acoustic pressure fields of extremely anisotropic metamaterials with (a),(c) sloping path and (b),(d) zigzag path at 6150 Hz for the domain 0.5 mm above the upper surface of the samples. Here, we set (a),(b) $|\alpha| = 30^\circ$ and (c),(d) $|\alpha| = 60^\circ$.

adjacent to the first region with a size of $120 \text{ mm} \cdot \sin \theta$ by 190 mm .

Meanwhile, the design of numerical simulations, which is based on the finite element method by COMSOL Multiphysics, is given in Fig. 11(a). Here, a point source is located 5 mm away from the sample to excite the SSAWs. The blue regions are PMLs. To show the design of the sample more clearly, we give the perspective of part of the sample in Fig. 11(b).

APPENDIX F: WAVE GUIDING WITH A REDUCED SIZE METAMATERIAL, AND SLOPING AND BACKSCATTERING-IMMUNE ZIGZAG PATHS WITH ARBITRARY ANGLES OF ROTATION

We first show that the SSAW-based EA AMM, even with a considerably reduced size ($l_{S2} = 1.6$ wavelength),

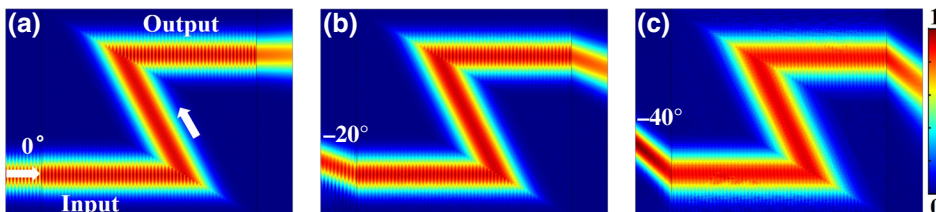


FIG. 15. The simulated pressure magnitude fields for (a) normal, (b) -20° , and (c) -40° incidence angles. Here, the bending angle is 60° . White arrows represent the direction of energy flow. The results are based on effective medium simulations.

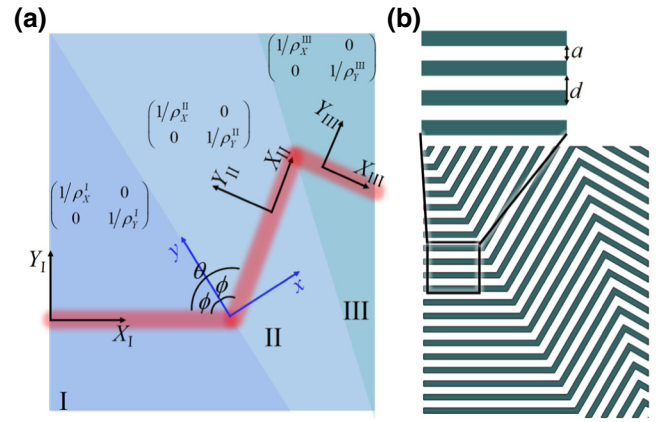


FIG. 14. (a) The 2D EAM with more general bent paths. Here, the mass density tensor for the three regions (I, II, and III) are shown in black letters in the (X, Y) coordinate system. (b) The corresponding bulk acoustic wave EA AMM design for the more general bending paths.

can still yield excellent performance. The simulation results are shown in Fig. 12, where the geometrical parameters are the same as those in Fig. 3(a).

To prove that the sloping and backscattering-immune zigzag paths of SSAWs are feasible for arbitrary angles of rotation, we give the pressure field distributions for HPSs and SPSs with $|\alpha| = 30^\circ$ and $|\alpha| = 60^\circ$ (shown in Fig. 13). The simulation results demonstrate robust wave guiding around sharp corners. Here, $d_1 = d_2 = 5 \text{ mm}$, $a_1 = a_2 = 4 \text{ mm}$, $h_1 = 12 \text{ mm}$, and $h_2 = 16 \text{ mm}$.

APPENDIX G: DIFFERENT BACKSCATTERING-IMMUNE WAVEGUIDES

In addition to the sawtooth-like 2D EAM in the main context of the paper, here we demonstrate that acoustic waves can also be guided along other types of paths, since any bending angle, θ , can be divided into two equal angles, in which different structures are occupied, as shown in Fig. 14(a). To design the backscattering-immune propagation at the interface between region I and region II, the y component of the global coordinate system [shown in blue in Fig. 14(a)] is parallel to the interface, and the X_i ($i = I, II$) components of the local coordinate system [shown in black in Fig. 14(a)] are in the directions of sound propagation.

The exactly identical mass density tensors $\overset{\leftrightarrow}{\rho}^{\text{diag}} (\rho_X^I = \rho_X^{II})$

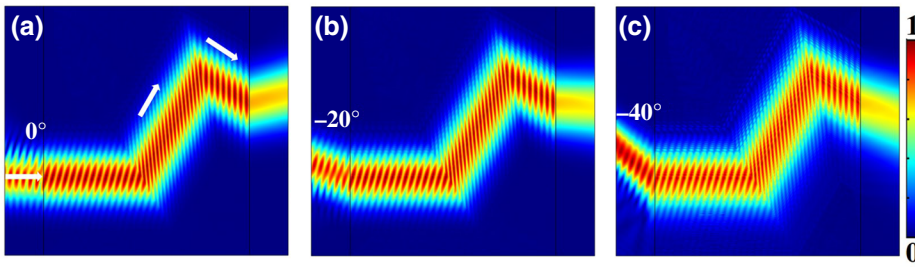


FIG. 16. The simulated pressure magnitude fields for (a) normal, (b) -20° , and (c) -40° incidence angles. Here, the bending angles are 120° and 90° . White arrows represent the direction of energy flow. The results are based on effective medium simulations.

and $\rho_Y^I = \rho_Y^{II}$) and bulk modulus, B , in the local coordinate systems should be satisfied. Furthermore, the rotation angles of the two regions in the global coordinate systems are $\alpha_I = -\pi/2 + \phi$ and $\alpha_{II} = \pi/2 - \phi$, respectively, which ensures backscattering-immune propagation around a sharp corner. The same operation can be utilized to design the mass density tensor and bulk modulus in region III. Figures 15 and 16 give the simulated sound pressure magnitude distributions for the two bent waveguides using the effective medium model, which demonstrates excellent performance in guiding the sound without scattering loss near the corners.

Meanwhile, simulations based on a type of periodic layered structure, which can be well described by homogenization theory [36], are also carried out to demonstrate the feasibility of controlling bulk acoustic waves using real structures. Figure 17(a) shows the simulation model with the same geometric parameters as those depicted in Fig. 14(b), where the period of PRB and the air gap are $d = 4$ mm and $a = 3.2$ mm, respectively. The corresponding effective parameters in the local coordinate system can

be written as [36]

$$\rho_X = \frac{d}{a}\rho_0, \rho_Y = \infty, \text{ and } B = \frac{d}{a}B_0, \quad (G1)$$

showing the nature of the extreme anisotropy for the proposed metamaterial. Figures 17 and 18 give the pressure field distributions along the path in Figs. 17(a) and 18(a), where different bending angles are introduced to illustrate the ability of low insertion loss propagation around corners.

We further consider the SSAW. The geometrical parameters of the unit cell are the same as those in Fig. 3(a). The pressure field distributions at a cut-plane located 0.5 mm above the sample are shown in Figs. 19 and 20. The acoustic wave is still strongly localized near the groove structures, although the thickness is greatly reduced; this is in good accordance with the aforementioned theoretical analysis. It should be noted that, for the SSAW design, the zigzag path must have the same bending angle throughout. This limitation is only for the SSAW design and is not a

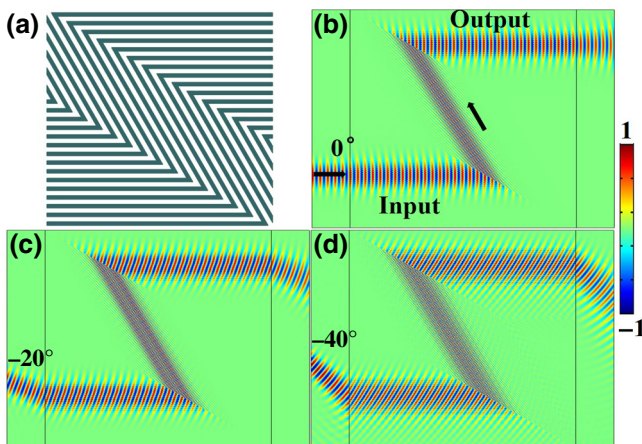


FIG. 17. Schematic illustration of an EA AMM with a zigzag path. Here, the bending angle is 60° . The simulated pressure fields for (b) normal, (c) -20° , and (d) -40° incidence angles. White arrows represent the direction of energy flow. The results are based on real-structure simulations.

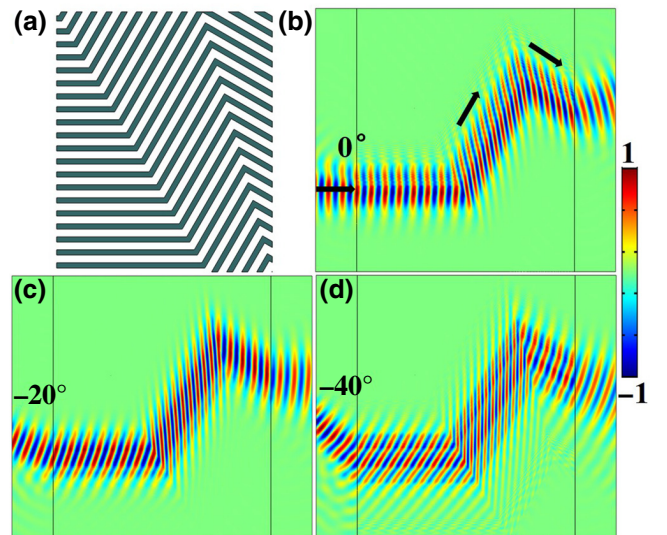


FIG. 18. (a) Schematic illustration of an EA AMM with a zigzag path. Here, the bending angles are 120° and 90° . The simulated pressure fields for (b) normal, (c) -20° , and (d) -40° incidence angles. White arrows represent the direction of energy flow. The results are based on real-structure simulations.

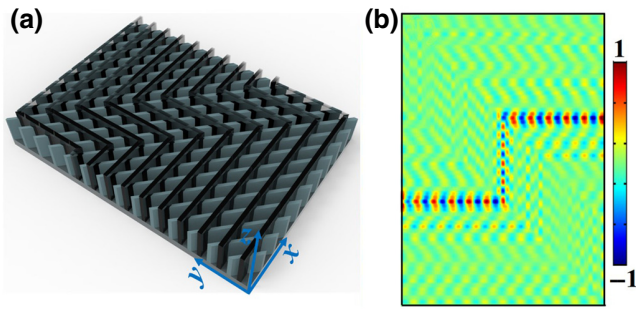


FIG. 19. (a) Schematic illustration of the 2D corrugated PRB with a zigzag path. Here, the bending angle is 90° . (b) The corresponding simulated pressure field distribution. The acoustic source is placed at the left end of the waveguide.

problem for the effective medium and bulk acoustic wave EA AMM models (as shown in Figs. 16 and 18).

APPENDIX H: BENDING ELECTROMAGNETIC WAVES AROUND SHARP CORNERS USING EXTREMELY ANISOTROPIC ELECTROMAGNETIC METAMATERIALS

To demonstrate backscattering-immune propagation of waves in extremely anisotropic electromagnetic metamaterials (EAEMMs), Fig. 21 gives the simulated wave field in an EAEMM with $\alpha_1 = -\alpha_2 = \alpha_3 = 45^\circ$, and $\alpha_1 = \alpha_2 = \alpha_3 = 45^\circ$ at 5 GHz under normal and -45° incidence angles. Here, the incident waves are transverse magnetic (TM) waves where $\vec{H} = (0, 0, 1)$. The sample is constructed by the periodic array of a stitching parallelogram perfect electromagnetic conductor (PEC), and the corresponding geometrical parameters satisfy $d = 4$ mm, $a = 3.2$ mm, $x_1 = 200$ mm, $x_2 = 400$ mm, and $x_3 = 600$ mm. Thus, the corresponding effective parameters satisfy [56]

$$\varepsilon_Y = d/a, \varepsilon_X = \varepsilon_Z = \infty, \mu_Y = 1, \mu_X = \mu_Z = 1/\varepsilon_Y. \quad (\text{H1})$$

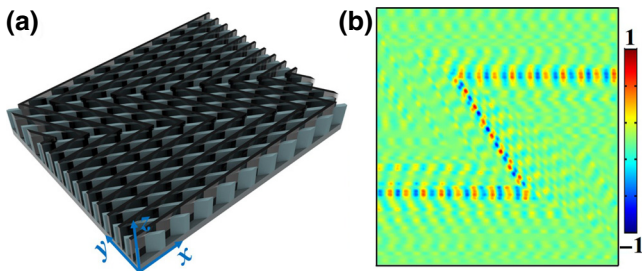


FIG. 20. (a) Schematic illustration of the 2D corrugated PRB with a zigzag path. Here, the bending angle is 60° . (b) The corresponding simulated pressure field distribution. The acoustic source is placed at the left end of the waveguide.

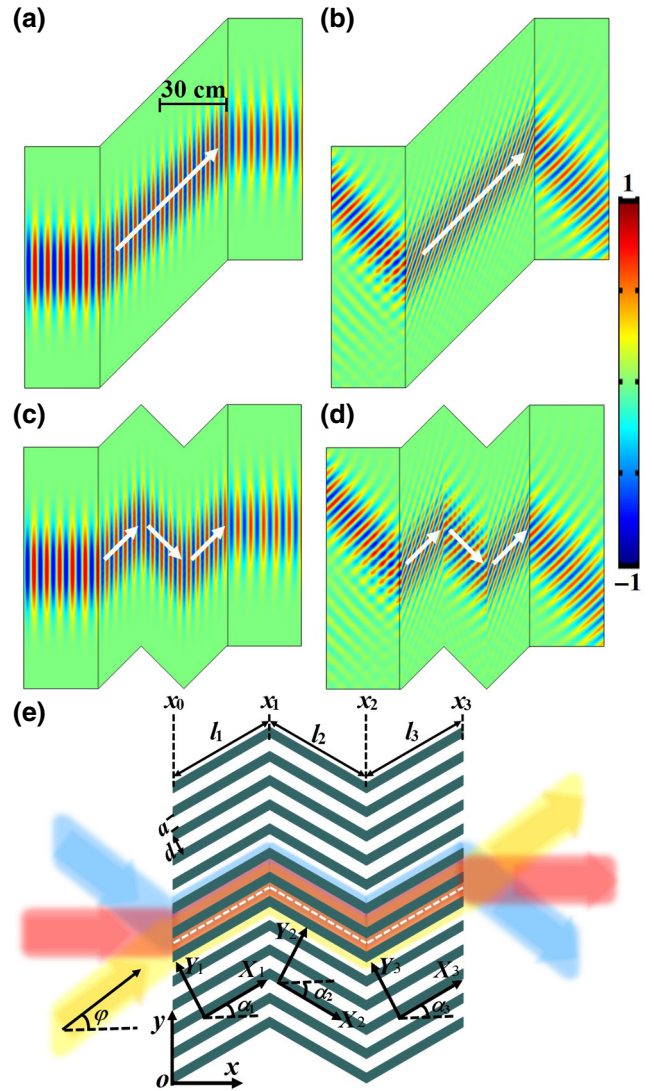


FIG. 21. Distribution of field component H_z of extremely anisotropic metamaterial with angles of rotation (a),(b) $\alpha_1 = \alpha_2 = \alpha_3 = 45^\circ$ and (c),(d) $\alpha_1 = -\alpha_2 = \alpha_3 = 45^\circ$ under (a),(c) normal and (b),(d) -45° incidence angles. The white arrows represent the direction of energy flow. (e) 2D configuration of EAEMM with bending path. Here, we set $d = 4$ mm, $a = 3.2$ mm, $x_1 = 200$ mm, $x_2 = 400$ mm, and $x_3 = 600$ mm. The operating frequency is 5 GHz.

It is easy to find that the direction of energy flow (white arrows in Fig. 21) depends only on the angle of rotation and no appreciable scattering is observed, even with the presence of sharp corners.

- [1] A. Khelif, A. Choujaa, S. Benchabane, B. Djafari-Rouhani, and V. Laude, Guiding and bending of acoustic waves in highly confined phononic crystal waveguides, *Appl. Phys. Lett.* **84**, 4400 (2004).

- [2] X. Li and Z. Liu, Bending and branching of acoustic waves in two-dimensional phononic crystals with linear defects, *Phys. Lett. A* **338**, 413 (2005).
- [3] T. Miyashita, Sonic crystals and sonic wave-guides, *Meas. Sci. Technol.* **16**, R47 (2005).
- [4] J.-H. Sun and T.-T. Wu, Propagation of surface acoustic waves through sharply bent two-dimensional phononic crystal waveguides using a finite-difference time-domain method, *Phys. Rev. B* **74**, 174305 (2006).
- [5] F.-L. Hsiao, A. Khelif, H. Moubchir, A. Choujaa, C.-C. Chen, and V. Laude, Waveguiding inside the complete band gap of a phononic crystal slab, *Phys. Rev. E* **76**, 056601 (2007).
- [6] M. Oudich, M. B. Assouar, and Z. Hou, Propagation of acoustic waves and waveguiding in a two-dimensional locally resonant phononic crystal plate, *Appl. Phys. Lett.* **97**, 193503 (2010).
- [7] A. Khelif and A. Adibi, *Phononic Crystals: Fundamentals and Applications* (Springer-Verlag, New York, 2015).
- [8] L.-Y. Wu, T.-Y. Chiang, C.-N. Tsai, M.-L. Wu, and L.-W. Chen, Design of an acoustic bending waveguide with acoustic metamaterials via transformation acoustics, *Appl. Phys. A* **109**, 523 (2012).
- [9] R. Fleury and A. Alù, Extraordinary Sound Transmission Through Density-Near-Zero Ultranarrow Channels, *Phys. Rev. Lett.* **111**, 055501 (2013).
- [10] M. Torres, F. M. De Espinosa, D. Garcia-Pablos, and N. Garcia, Sonic Band Gaps in Finite Elastic Media: Surface States and Localization Phenomena in Linear and Point Defects, *Phys. Rev. Lett.* **82**, 3054 (1999).
- [11] A. B. Khanikaev, R. Fleury, S. H. Mousavi, and A. Alu, Topologically robust sound propagation in an angular-momentum-biased graphene-like resonator lattice, *Nat. Commun.* **6**, 8260 (2015).
- [12] Z. Yang, F. Gao, X. Shi, X. Lin, Z. Gao, Y. Chong, and B. Zhang, Topological Acoustics, *Phys. Rev. Lett.* **114**, 114301 (2015).
- [13] Y.-G. Peng, C.-Z. Qin, D.-G. Zhao, Y.-X. Shen, X.-Y. Xu, M. Bao, H. Jia, and X.-F. Zhu, Experimental demonstration of anomalous Floquet topological insulator for sound, *Nat. Commun.* **7**, 13368 (2016).
- [14] C. He, X. Ni, H. Ge, X.-C. Sun, Y.-B. Chen, M.-H. Lu, X.-P. Liu, and Y.-F. Chen, Acoustic topological insulator and robust one-way sound transport, *Nat. Phys.* **12**, 1124 (2016).
- [15] J. Lu, C. Qiu, L. Ye, X. Fan, M. Ke, F. Zhang, and Z. Liu, Observation of topological valley transport of sound in sonic crystals, *Nat. Phys.* **13**, 369 (2017).
- [16] A. Souslov, B. C. Van Zuiden, D. Bartolo, and V. Vitelli, Topological sound in active-liquid metamaterials, *Nat. Phys.* **13**, 1091 (2017).
- [17] Y. Deng, H. Ge, Y. Tian, M. Lu, and Y. Jing, Observation of zone folding induced acoustic topological insulators and the role of spin-mixing defects, *Phys. Rev. B* **96**, 184305 (2017).
- [18] X. Zhang, M. Xiao, Y. Cheng, M.-H. Lu, and J. Christensen, Topological sound, *Commun. Phys.* **1**, 97 (2018).
- [19] Z. Zhang, Y. Tian, Y. Wang, S. Gao, Y. Cheng, X. Liu, and J. Christensen, Directional acoustic antennas based on valley-hall topological insulators, *Adv. Mater.* **30**, 1803229 (2018).
- [20] Z. Zhang, Y. Tian, Y. Cheng, Q. Wei, X. Liu, and J. Christensen, Topological Acoustic Delay Line, *Phys. Rev. Appl.* **9**, 034032 (2018).
- [21] F. Z. Nejad and R. Fleury, Topological analog signal processing, *Nat. Commun.* **10**, 2058 (2019).
- [22] F. Z. Nejad and R. Fleury, Topological Fano Resonances, *Phys. Rev. Lett.* **122**, 014301 (2019).
- [23] Z. Liu, X. Zhang, Y. Mao, Y. Zhu, Z. Yang, C. T. Chan, and P. Sheng, Locally resonant sonic materials, *Science* **289**, 1734 (2000).
- [24] J. Li and C. T. Chan, Double-negative acoustic metamaterial, *Phys. Rev. E* **70**, 055602 (2004).
- [25] N. Fang, D. Xi, J. Xu, M. Ambati, W. Srituravanich, C. Sun, and X. Zhang, Ultrasonic metamaterials with negative modulus, *Nat. Mater.* **5**, 452 (2006).
- [26] Y. Ding, Z. Liu, C. Qiu, and J. Shi, Metamaterial with Simultaneously Negative Bulk Modulus and Mass Density, *Phys. Rev. Lett.* **99**, 093904 (2007).
- [27] Z. Liang and J. Li, Extreme Acoustic Metamaterial by Coiling up Space, *Phys. Rev. Lett.* **108**, 114301 (2012).
- [28] Y. Xie, B.-I. Popa, L. Zigoneanu, and S. A. Cummer, Measurement of a Broadband Negative Index with Space-Coiling Acoustic Metamaterials, *Phys. Rev. Lett.* **110**, 175501 (2013).
- [29] H. Ge, M. Yang, C. Ma, M.-H. Lu, Y.-F. Chen, N. Fang, and P. Sheng, Breaking the barriers: Advances in acoustic functional materials, *Natl. Sci. Rev.* **5**, 159 (2017).
- [30] C. Shen, J. Xu, N. X. Fang, and Y. Jing, Anisotropic Complementary Acoustic Metamaterial for Canceling out Aberating Layers, *Phys. Rev. X* **4**, 041033 (2014).
- [31] F. Z. Nejad and R. Fleury, Performing mathematical operations using high-index acoustic metamaterials, *New J. Phys.* **20**, 073001 (2018).
- [32] Y. Fu, C. Shen, Y. Cao, L. Gao, H. Chen, C. T. Chan, S. A. Cummer, and Y. Xu, Reversal of transmission and reflection based on acoustic metagratings with integer parity design, *Nat. Commun.* **10**, 2326 (2019).
- [33] C. Shen, Y. Xie, N. Sui, W. Wang, S. A. Cummer, and Y. Jing, Broadband Acoustic Hyperbolic Metamaterial, *Phys. Rev. Lett.* **115**, 254301 (2015).
- [34] J. Zhu, J. Christensen, J. Jung, L. Martin-Moreno, X. Yin, L. Fok, X. Zhang, and F. Garcia-Vidal, A holey-structured metamaterial for acoustic deep-subwavelength imaging, *Nat. Phys.* **7**, 52 (2011).
- [35] L. Zigoneanu, B.-I. Popa, and S. A. Cummer, Three-dimensional broadband omnidirectional acoustic ground cloak, *Nat. Phys.* **13**, 352 (2014).
- [36] J. Li, L. Fok, X. Yin, G. Bartal, and X. Zhang, Experimental demonstration of an acoustic magnifying hyperlens, *Nat. Mater.* **8**, 931 (2009).
- [37] Y. Chen, H. Liu, M. Reilly, H. Bae, and M. Yu, Enhanced acoustic sensing through wave compression and pressure amplification in anisotropic metamaterials, *Nat. Commun.* **5**, 5247 (2014).
- [38] X. Zhou and G. Hu, Superlensing effect of an anisotropic metamaterial slab with near-zero dynamic mass, *Appl. Phys. Lett.* **98**, 263510 (2011).
- [39] L. Kelders, J. F. Allard, and W. Lauriks, Ultrasonic surface waves above rectangular-groove gratings, *J. Acoust. Soc. Am.* **103**, 2730 (1998).

- [40] Z. He, H. Jia, C. Qiu, Y. Ye, R. Hao, M. Ke, and Z. Liu, Nonleaky surface acoustic waves on a textured rigid surface, *Phys. Rev. B* **83**, 132101 (2011).
- [41] J. Zhu, Y. Chen, X. Zhu, F. J. Garcia-Vidal, X. Yin, W. Zhang, and X. Zhang, Acoustic rainbow trapping, *Sci. Rep.* **3**, 1728 (2013).
- [42] J. Lu, C. Qiu, M. Ke, and Z. Liu, Directional excitation of the designer surface acoustic waves, *Appl. Phys. Lett.* **106**, 201901 (2015).
- [43] L. T. Wu, G. Y. Song, W. K. Cao, Q. Cheng, T. J. Cui, and Y. Jing, Generation of multiband spoof surface acoustic waves via high-order modes, *Phys. Rev. B* **97**, 214305 (2018).
- [44] D. Zhao, Z. Liu, C. Qiu, Z. He, F. Cai, and M. Ke, Surface acoustic waves in two-dimensional phononic crystals: Dispersion relation and the eigenfield distribution of surface modes, *Phys. Rev. B* **76**, 144301 (2007).
- [45] Z. He, X. Li, J. Mei, and Z. Liu, Improving imaging resolution of a phononic crystal lens by employing acoustic surface waves, *J. Appl. Phys.* **106**, 026105 (2009).
- [46] D. Torrent and J. Sánchez-Dehesa, Acoustic Analogue of Graphene: Observation of Dirac Cones in Acoustic Surface Waves, *Phys. Rev. Lett.* **108**, 174301 (2012).
- [47] Y. Ye, M. Ke, Y. Li, T. Wang, and Z. Liu, Focusing of spoof surface-acoustic-waves by a gradient-index structure, *J. Appl. Phys.* **114**, 154504 (2013).
- [48] S. Yves, R. Fleury, F. Lemoult, M. Fink, and G. Lerosey, Topological acoustic polaritons: Robust sound manipulation at the subwavelength scale, *New J. Phys.* **19**, 075003 (2017).
- [49] T. Liu, X. Zhu, F. Chen, S. Liang, and J. Zhu, Unidirectional Wave Vector Manipulation in Two-Dimensional Space with an all Passive Acoustic Parity-Time-Symmetric Metamaterials Crystal, *Phys. Rev. Lett.* **120**, 124502 (2018).
- [50] T. Liu, F. Chen, S. J. Liang, H. Gao, and J. Zhu, Subwavelength Sound Focusing and Imaging Via Gradient Metasurface-Enabled Spoof Surface Acoustic Wave Modulation, *Phys. Rev. Appl.* **11**, 034061 (2019).
- [51] A. Castanié, J.-F. Mercier, S. Felix, and A. Maurel, Generalized method for retrieving effective parameters of anisotropic metamaterials, *Opt. Express* **22**, 29937 (2014).
- [52] D. Smith and D. Schurig, Electromagnetic Wave Propagation in Media with Indefinite Permittivity and Permeability Tensors, *Phys. Rev. Lett.* **90**, 077405 (2003).
- [53] R. Fleury, D. L. Sounas, and A. Alu, Negative Refraction and Planar Focusing Based on Parity-Time Symmetric Metasurfaces, *Phys. Rev. Lett.* **113**, 023903 (2014).
- [54] H. He, C. Qiu, L. Ye, X. Cai, X. Fan, M. Ke, F. Zhang, and Z. Liu, Topological negative refraction of surface acoustic waves in a Weyl phononic crystal, *Nature* **560**, 61 (2018).
- [55] Y. Deng, M. Lu, and Y. Jing, A comparison study between acoustic topological states based on valley Hall and quantum spin Hall effects, *J. Acoust. Soc. Am.* **146**, 721 (2019).
- [56] F. Garcia-Vidal, L. Martin-Moreno, and J. Pendry, Surfaces with holes in them: New plasmonic metamaterials, *J. Opt. A: Pure Appl. Opt.* **7**, S97 (2005).